東北大学機関リポジトリ
TOUR
Tohoku University Repository

東北大学

Tensile Characterization of Carbon Nanotube-Reinforced Polymer Composites at Cryogenic Temperatures: Experiments and Multiscale Simulations

Tensile Characterization of Carbon Nanotube-Reinforced Polymer Composites at Cryogenic Temperatures: Experimens and Multiscale Simulations

Tomo Takeda, Yasuhide Shindo, Fumio Narita and Yuya Mito*

Department of Materials Processing, Graduate School of Engineering, Tohoku University, Sendai 980-8579, Japan

The purpose of this research is to experimentally and numerically evaluate the mechanical performance of carbon nanotube (CNT)-reinforced polymer composites subjected to tension in a cryogenic environment. Cryogenic tensile tests were conducted on CNT/polycarbonate composites to identify the effects of CNTs on their tensile properties. Finite element computations were also conducted using a model for the representative volume element (RVE) of CNT-reinforced composites in order to determine the effective composite elastic modulus and the stress state within the composites. The possible existence of the imperfect interface bonding between the CNT and the matrix was considered in the finite element model. The CNT properties used in the analysis were obtained by employing an analytical molecular structural mechanics model. The numerical findings were then correlated with the experimental results. [doi:10.2320/matertrans.MBW200817]

1. Introduction

The discovery of carbon nanotubes (CNTs) in 1991[1] has stimulated considerable interest in the investigation of the physical and mechanical properties of their novel materials and their potential technological applications. CNTs exist as either single-walled or multi-walled structures.[2] A single-walled nanotube (SWNT) is described as a rolled-up tubular shell of graphene sheet. In contrast, a multi-walled nanotube (MWNT) is composed of a set of coaxially situated SWNTs of different radii. CNTs possess unique mechanical, electrical, magnetic, optical and thermal properties.[3] For example, the elastic modulus and strength of CNTs ranging about 0.3–1 TPa and 10–500 GPa, respectively, have been reported.[4] These properties as well as their high aspect ratio and low density suggest that CNTs are excellent candidates for nano-reinforcing a variety of materials, and many material properties and features can be modified.[5]

Polymeric materials have been of significant importance to the engineering community for many years. Polymers have been used in many cryogenic applications (e.g., structural parts, seals, spacecraft fuel storage tank liners).[6] Another use of polymers is for matrix materials of cryogenic composites.[7] This has placed increasing demands on the mechanical performance of polymeric materials and CNT-reinforced polymer composites therefore appear to have potential for cryogenic service (e.g., ultra-lightweight cryogenic fuel tanks of reusable launch vehicles). In fact, since CNTs have been appreciated as strong reinforcements for advanced materials for aerospace applications, these materials must be able to survive in a cryogenic environment without apparently generating any structural degradation.[8] In order to fully explore the potential of CNT-reinforced polymer composites for cryogenic applications, a thorough understanding of their mechanical behavior at cryogenic temperatures is necessary.

There have been numerous theoretical and experimental research related to the CNTs and their co-related polymer based composites since the discovery of CNTs. Several review articles have been published[9–11] which summarize the research work on the structure and processing of CNTs, as well as characterization and modeling of CNTs and their composites. Although CNT-reinforced polymer composites are an obvious materials application area, there have not been many successful experiments, which show the advantage of using CNTs as reinforcements over traditional carbon fibers.[12] This may be caused by a variety of factors (e.g., CNT dispersion within the polymer, size, shape and orientation of CNTs, type of CNTs used),[13,14] and the main problem is in creating a good interface bonding between CNTs and the surrounding polymer matrix.[15] A poor interface bonding could be a limiting factor for good load transfer from the matrix to the CNTs during loading. In addition, very few studies have been reported on the cryogenic mechanical response of CNT-reinforced polymer composites, and, as a result, the CNT reinforcement efficiency in a cryogenic environment is still not well understood.

This paper focuses on understanding the cryogenic tensile response of CNT-reinforced polymer composites. Tensile tests were performed at room temperature and liquid nitrogen temperature (77 K) on the composites based on the MWNTs with the polycarbonate, and the effects of CNT addition on their tensile properties were evaluated. Finite element simulations were also performed to predict the effective elastic modulus of CNT/polycarbonate composites and the stress state within the composites. Three-dimensional finite elements were used to model the representative volume element (RVE) of the composites, and the possible existence of the imperfect CNT/matrix interface bonding was considered. An analytical molecular structural mechanics model was employed to estimate the CNT properties. The numerical predictions were then compared with the experimental observations and the results are discussed to give some insights into the reinforcing mechanisms in the composites at cryogenic temperatures.

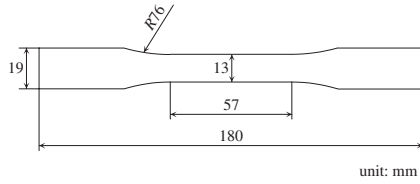*Graduate Student, Tohoku University

Fig. 1 Geometry and dimensions of tensile test specimen.

2. Experimental Procedure

2.1 Material and specimen preparation

In this work, composite materials consisting of MWNTs and a polycarbonate matrix were considered. The MWNT/polycarbonate composite samples were manufactured by a commercial supplier. Neat polycarbonate samples were also prepared. The MWNT diameters ranged from 10 to 40 nm, and the MWNT lengths ranged from 5 to 20 μm. The composite samples contained MWNT weight fractions of 1.5, 2.5 and 5 mass%. The conversion of CNT weight fraction W^N to CNT volume fraction V^N can be performed by using the following equation:[14]

$$V^N = \frac{W^N \rho^M}{W^N \rho^M + (1 - W^N)\rho^N}, \tag{1}$$

where ρ^N and ρ^M are the densities of the CNT and matrix, respectively. The superscripts N and M refer to CNT and matrix, respectively. The density of the neat polycarbonate taken from the supplier's data is $1.2\,g/cm^3$, and a typical value of the density for a MWNT is $1.8\,g/cm^3$.[4] The calculated values of V^N for the MWNT/polycarbonate composites containing 1.5, 2.5 and 5 mass% MWNTs are 1.0, 1.7 and 3.4 vol%, respectively.

The dogbone-shaped specimens for tensile tests were machined from the sample plates to the dimensions recommended by ASTM D 638.[16] The as-received thickness of the plates was about 3 mm for the neat polycarbonate samples, and about 2.7 mm for the MWNT/polycarbonate composite samples. The geometry and dimensions of the tensile test specimen are shown in Fig. 1.

2.2 Tensile tests

Tensile tests were performed on a 30 kN capacity servo-hydraulic testing machine under displacement control. The displacement rate used was 0.6 mm/min. The specimens were tested at room temperature and liquid nitrogen temperature (77 K). In cryogenic engineering, liquid nitrogen is often employed as cooling media.[7] The tensile testing at 77 K was conducted with specimens immersed in liquid nitrogen at atmospheric pressure in a dewar. Load and displacement were measured continually throughout each test. The extensometer was used for axial strain measurements. Stress-strain behavior of the neat polycarbonate and MWNT/polycarbonate composite samples was recorded, and their Young's modulus, 0.2% offset yield strength, ultimate tensile strength and strain-to-failure were determined according to ASTM D 638. The tensile stress was calculated by dividing the applied load by the average cross-sectional area in the specimen gage section. Also, separate tests were conducted to determine the Poisson's ratios of the

neat polycarbonate at room temperature and 77 K. Axial and transverse strains were measured using electrical resistance strain gages that were mounted at the center of the gage sections on both sides of the specimens. In practice, three specimens were tested for each material and condition. After tensile testing, the fracture surfaces of the specimens were examined by scanning electron microscopy (SEM). For SEM observation, a thin layer of carbon was coated onto the fracture surfaces.

3. Multiscale Analysis

3.1 Constituent material properties

In this study, the elastic properties of a CNT were calculated based on molecular structural mechanics (MSM) and subsequently, the CNT was treated as an equivalent solid cylinder. The similar approach was used by Gao and Li.[17] The CNTs considered were MWNTs. Molecular dynamic simulations of MWNTs subjected to uniaxial tension have shown that the inner layers of the MWNTs do not contribute much to their elastic properties.[18] Hence, the elastic properties of the MWNTs used in composites can be estimated by regarding the outermost layer as a SWNT, i.e., the elastic properties of MWNTs in composites are equivalent to those of a SWNT with the same outermost diameter.[11] Based on this finding, the analytical MSM model for simulation of SWNTs developed by Xiao et al.[19] was employed here to calculate Young's modulus and Poisson's ratio of the MWNTs. A brief summary of the model is given below.

The atomic structure of CNTs can be described in terms of the tube chirality (n_1, n_2), where n_1 and n_2 are a pair of two integers. The variation of the chirality (n_1, n_2) results in different types of CNTs, and two main types of CNTs, i.e., armchair $(n_1 = n_2)$ and zigzag $(n_2 = 0)$, are considered in the model. The CNT radius R^N can be calculated as follows:

$$R^N = \frac{b}{2\pi}\{3(n_1^2 + n_1 n_2 + n_2^2)\}^{1/2}, \tag{2}$$

where b is the C–C bond length (0.142 nm). The model incorporates the modified Morse potential function to describe the C–C bond in a CNT, and the total potential energy U can be expressed as the sum of the energies due to bond stretch Δb and bond angle variation $\Delta \theta$

$$U = D[\{1 - \exp(-\beta \Delta b)\}^2 - 1] + \frac{1}{2}k_{\theta 1}\Delta\theta^2(1 + k_{\theta 2}\Delta\theta^4), \tag{3}$$

where $D = 0.6031$ nN·nm, $\beta = 26.25$ nm^{-1}, $k_{\theta 1} = 1.42$ nN·nm/rad^2, and $k_{\theta 2} = 0.754$ rad^{-4}. Under loading, forces and moments acting on the carbon atoms are obtained as

$$F(\Delta b) = 2\beta D\{1 - \exp(-\beta \Delta b)\}\exp(-\beta \Delta b), \tag{4}$$

$$M(\Delta\theta) = k_{\theta 1}\Delta\theta\{1 + 3k_{\theta 2}\Delta\theta^4\}, \tag{5}$$

by differentiating the total potential energy U. Based on the force and moment equilibrium conditions and the geometry of the CNT structure, the stress-strain curves for SWNTs can be obtained. The model is capable of predicting Young's modulus and Poisson's ratio as a function of the CNT diameter $2R^N$. In the model, CNTs are simulated as defect-free materials neglecting the effect of initial defects.
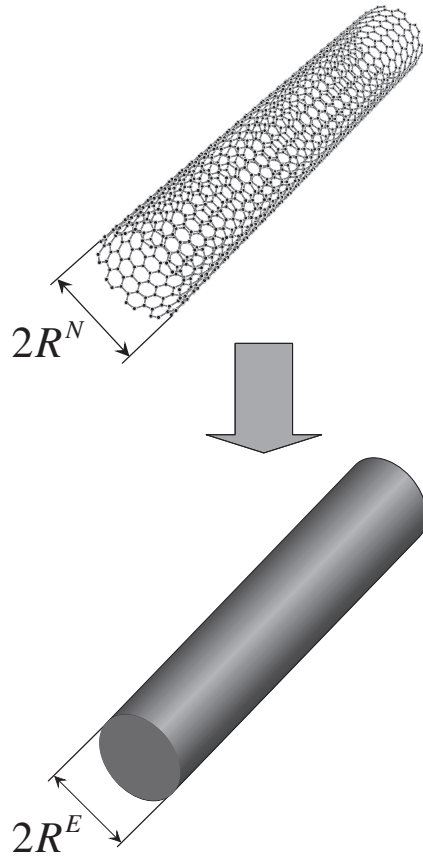
$$2R^N$$

$$2R^E$$

Fig. 2　Effective CNT.

In the application of the analytical MSM model, the outermost diameter $2R^N$ of the MWNTs in the composites was assumed to be 25 nm. Young's moduli and Poisson's ratios of SWNTs with diameters of about 25 nm from the model were found to be insensitive to their chirality, and the predicted Young's modulus E_{MSM} and Poisson's ratio ν_{MSM} are 1.13 TPa and 0.20, respectively. With the elastic properties of the CNT determined based on its atomic structure (E_{MSM}, ν_{MSM}), the CNT embedded in the matrix can then be replaced by an equivalent solid cylinder (effective CNT) with the diameter $2R^E = 2R^N$ (see Fig. 2). The superscript E denotes the effective CNT. The Young's modulus E^E and Poisson's ratio ν^E of the effective CNT can be obtained as[17]

$$E^E = \frac{R^{N2} - (R^N - t^N)^2}{R^{N2}} E_{MSM},\qquad(6)$$

$$\nu^E = \nu_{MSM},\qquad(7)$$

where t^N is the tube wall thickness and has been commonly assumed to be the interlayer spacing of graphite (0.34 nm).[20] With both the radius R^N and the wall thickness t^N of the CNT involved in eq. (6) as two independent variables, the hollowness of the CNT is directly incorporated in the determination of E^E. In the present study, the effective CNT was assumed to have isotropic elastic properties, i.e., Young's modulus E^E, Poisson's ratio ν^E and shear modulus $G^E = E^E/2(1 + \nu^E)$.[17] Also, the elastic properties of the effective CNT were assumed to be unaffected by temperature.[21] In addition, since the coefficients of thermal expansion (CTEs) of CNTs have

not yet been thoroughly investigated, the CTEs of graphite in the plane of a graphene sheet (-1.2×10^{-6}/K) and in the out-of-plane direction (25.9×10^{-6}/K) at room temperature[22] were used as the longitudinal and transverse CTEs α_l^E, α_t^E of the effective CNT, respectively. The subscripts l and t stand for the longitudinal and transverse directions, respectively. This assumption is reasonable because of the relative similarity between graphite and CNTs.[23]

The polycarbonate was taken as an isotropic material with its elastic and thermal properties depending upon temperature Φ. The Young's modulus $E^M(\Phi)$ and Poisson's ratio $\nu^M(\Phi)$ of the polycarbonate were determined from the tensile tests performed at room temperature and 77 K, and its shear modulus $G^M(\Phi)$ was calculated from $G^M(\Phi) = E^M(\Phi)/2\{1 + \nu^M(\Phi)\}$. Also, the CTE of the polycarbonate $\alpha^M(\Phi)$ was approximated by the following exponential function based on the experimental data for its thermal expansion:[6]

$$\alpha^M(\Phi) = 9.378 \exp(7.578 \times 10^{-3}\Phi) \ [10^{-6}/K].\qquad(8)$$

3.2　Finite element simulations of the composite RVE

The RVE of CNT-reinforced composites was chosen as a computational model. The RVE model is shown in Fig. 3, where the effective CNT embedded in the matrix is regarded as located at the center of the RVE. The model includes an isotropic interfacial layer with Young's modulus $E^I(\Phi) = \chi E^M(\Phi)$ ($0 < \chi \leq 1$), Poisson's ratio $\nu^I(\Phi) = \nu^M(\Phi)$, shear modulus $G^I(\Phi) = E^I(\Phi)/2\{1 + \nu^I(\Phi)\}$ and CTE $\alpha^I(\Phi) = \alpha^M(\Phi)$, in order to represent the imperfection in the CNT/matrix interface. The superscript I represents the interfacial layer. The local Cartesian coordinate system (x, y, z) is set up such that the x-axis is in the longitudinal direction, and the y- and z-axes are in the transverse plane of the RVE. In
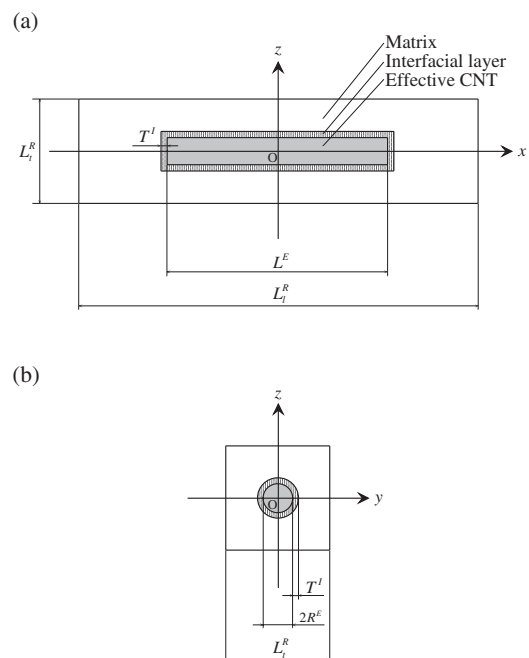
Fig. 3　RVE of CNT-reinforced composites: (a) $y = 0$ plane; (b) $x = 0$ plane.

accordance with the figure, L^E represents the length of the effective CNT, T^I denotes the thickness of the interfacial layer, whereas L_l^R and L_t^R are used to represent the RVE lengths in the longitudinal and transverse directions, respectively. The superscript R denotes the RVE. In the RVE model, the effective CNT aspect ratio $L^E/2R^E$ was assumed to be equal to the RVE aspect ratio L_l^R/L_t^R,[24] and the interfacial layer thickness T^I was assumed to be $0.05R^E$. The volume fraction of the effective CNT in the RVE V^E can be expressed as:

$$V^E = 2\pi \left(\frac{R^E}{L_t^R} \right)^3. \tag{9}$$

The effective CNT volume fraction in the RVE V^E

corresponds to the CNT volume fraction in the composite V^N.

The RVE was subjected to the mechanical and thermal loads. The thermal load represents the difference between the stress-free temperature Φ_s and the current temperature Φ, i.e., $\Phi - \Phi_s$. For the polycarbonate, a typical value of the glass transition temperature is 406 K.[25] The manufacturing temperature of the MWNT/polycarbonate composites, 553 K (provided by the supplier), is higher than the glass transition temperature. Hence, the stress-free temperature Φ_s in the finite element calculations was taken to be equal to 406 K.

The constitutive equations for the RVE constituents are:

$$\begin{bmatrix} \varepsilon_{xx}^\delta(x,y,z) - \varepsilon_{xxT}^\delta(\Phi) \\ \varepsilon_{yy}^\delta(x,y,z) - \varepsilon_{yyT}^\delta(\Phi) \\ \varepsilon_{zz}^\delta(x,y,z) - \varepsilon_{zzT}^\delta(\Phi) \\ 2\varepsilon_{yz}^\delta(x,y,z) \\ 2\varepsilon_{zx}^\delta(x,y,z) \\ 2\varepsilon_{xy}^\delta(x,y,z) \end{bmatrix} = \begin{bmatrix} 1/E^\delta & -\nu^\delta/E^\delta & -\nu^\delta/E^\delta & 0 & 0 & 0 \\ -\nu^\delta/E^\delta & 1/E^\delta & -\nu^\delta/E^\delta & 0 & 0 & 0 \\ -\nu^\delta/E^\delta & -\nu^\delta/E^\delta & 1/E^\delta & 0 & 0 & 0 \\ 0 & 0 & 0 & 1/G^\delta & 0 & 0 \\ 0 & 0 & 0 & 0 & 1/G^\delta & 0 \\ 0 & 0 & 0 & 0 & 0 & 1/G^\delta \end{bmatrix} \begin{bmatrix} \sigma_{xx}^\delta(x,y,z) \\ \sigma_{yy}^\delta(x,y,z) \\ \sigma_{zz}^\delta(x,y,z) \\ \sigma_{yz}^\delta(x,y,z) \\ \sigma_{zx}^\delta(x,y,z) \\ \sigma_{xy}^\delta(x,y,z) \end{bmatrix},$$
$$(\delta = E, M, I), \tag{10}$$

where $\varepsilon_{xx}^\delta(x,y,z)$, $\varepsilon_{yy}^\delta(x,y,z)$, $\varepsilon_{zz}^\delta(x,y,z)$, $\varepsilon_{yz}^\delta(x,y,z)$, $\varepsilon_{zx}^\delta(x,y,z)$, $\varepsilon_{xy}^\delta(x,y,z)$ are the strain components, $\varepsilon_{xxT}^\delta(\Phi)$, $\varepsilon_{yyT}^\delta(\Phi)$, $\varepsilon_{zzT}^\delta(\Phi)$ are the thermal strain components, and $\sigma_{xx}^\delta(x,y,z)$, $\sigma_{yy}^\delta(x,y,z)$, $\sigma_{zz}^\delta(x,y,z)$, $\sigma_{yz}^\delta(x,y,z)$, $\sigma_{zx}^\delta(x,y,z)$, $\sigma_{xy}^\delta(x,y,z)$ ($\delta = E, M, I$) are the stress components. The thermal strain components $\varepsilon_{xxT}^\delta(\Phi)$, $\varepsilon_{yyT}^\delta(\Phi)$, $\varepsilon_{zzT}^\delta(\Phi)$ ($\delta = E, M, I$) are given by

$$\varepsilon_{xxT}^E(\Phi) = \alpha_l^E(\Phi - \Phi_s), \quad \varepsilon_{yyT}^E(\Phi) = \varepsilon_{zzT}^E(\Phi) = \alpha_t^E(\Phi - \Phi_s), \tag{11}$$

$$\varepsilon_{xxT}^\delta(\Phi) = \varepsilon_{yyT}^\delta(\Phi) = \varepsilon_{zzT}^\delta(\Phi) = \int_{\Phi_s}^{\Phi} \alpha^\delta(\phi)d\phi, \quad (\delta = M, I). \tag{12}$$

The RVE of CNT-reinforced composites can be assumed to be transversely isotropic, with the plane of isotropy being the y-z plane (see Fig. 3). For the transversely isotropic RVE, there are five independent elastic properties: longitudinal Young's modulus E_l^R, transverse Young's modulus E_t^R, longitudinal Poisson's ratio ν_{lt}^R, transverse Poisson's ratio ν_{tt}^R, and longitudinal shear modulus $G_{lt}^R = G_{tl}^R$. The Poisson's ratio ν_{lt}^R reflects shrinkage (expansion) in the transverse direction, due to tensile (compressive) stress in the longitudinal direction. In addition, the transverse shear modulus G_{tt}^R is related to the transverse Young's modulus E_t^R and Poisson's ratio ν_{tt}^R by $G_{tt}^R = E_t^R/2(1 + \nu_{tt}^R)$. The longitudinal Young's modulus E_l^R and Poisson's ratio ν_{lt}^R, transverse Young's modulus E_t^R and Poisson's ratio ν_{tt}^R, and longitudinal shear modulus $G_{lt}^R = G_{tl}^R$ can be obtained from the finite element simulations of the RVE under longitudinal normal, transverse normal, and longitudinal shear loadings, respectively. Note that the difference between the bending rigidity in a solid cylinder (effective CNT) and that in a thin-walled hollow cylinder (actual CNT) seems to have little effect on the RVE response under these loading conditions. The method employed in this study was adapted from the approach used by Sun and Vaidya.[26]

For longitudinal and transverse normal loadings, due to the symmetry only one-eighth of the RVE ($0 \leq x \leq L_l^R/2$, $0 \leq y \leq L_t^R/2$, $0 \leq z \leq L_t^R/2$) was considered. Let the displacement components in the x-, y- and z-directions be labeled by $u_x^\delta(x,y,z)$, $u_y^\delta(x,y,z)$ and $u_z^\delta(x,y,z)$ ($\delta = E, M, I$), respectively. The displacement boundary conditions for the RVE under normal load in the longitudinal (x-) direction are:

$$\left. \begin{aligned} u_x^\delta(0,y,z) &= 0, \\ u_x^M(L_l^R/2,y,z) &= u_x^*, \end{aligned} \right\} 0 \leq y \leq \frac{L_t^R}{2}, \ 0 \leq z \leq \frac{L_t^R}{2}, \quad (\delta = E, M, I), \tag{13}$$

$$\left. \begin{aligned} u_y^\delta(x,0,z) &= 0, \\ u_y^M(x,L_t^R/2,z) &= u_y^0, \end{aligned} \right\} 0 \leq x \leq \frac{L_l^R}{2}, \ 0 \leq z \leq \frac{L_t^R}{2}, \quad (\delta = E, M, I), \tag{14}$$

$$\left. \begin{aligned} u_z^\delta(x,y,0) &= 0, \\ u_z^M(x,y,L_t^R/2) &= u_z^0, \end{aligned} \right\} 0 \leq x \leq \frac{L_l^R}{2}, \ 0 \leq y \leq \frac{L_t^R}{2}, \quad (\delta = E, M, I), \tag{15}$$

where u_x^* is the uniform displacement in the x-direction, and u_y^0 and u_z^0 are the uniform displacements in the y- and z-directions determined from the following conditions:

$$\left.\begin{array}{l} \dfrac{\displaystyle\int_0^{L_t^R/2}\int_0^{L_l^R/2}\sigma_{yy}^M(x,L_t^R/2,z)dxdz}{(L_l^R/2)(L_t^R/2)} = 0, \quad \text{(for the uniform displacement } u_y^0), \\[2em] \dfrac{\displaystyle\int_0^{L_t^R/2}\int_0^{L_l^R/2}\sigma_{zz}^M(x,y,L_t^R/2)dxdy}{(L_l^R/2)(L_t^R/2)} = 0, \quad \text{(for the uniform displacement } u_z^0). \end{array}\right\} \tag{16}$$

The longitudinal Young's modulus $E_l^R = E_x^R$ and Poisson's ratio $\nu_{lt}^R = \nu_{xy}^R = \nu_{xz}^R$ are given by

$$E_l^R = E_x^R = \frac{\sigma_{xx}^*}{(u_x^* - u_{xT}^*)/(L_l^R/2)}, \tag{17}$$

$$\nu_{lt}^R = \begin{cases} \nu_{xy}^R = -\dfrac{(u_y^0 - u_{yT}^0)/(L_t^R/2)}{(u_x^* - u_{xT}^*)/(L_l^R/2)}, \\[1.5em] \nu_{xz}^R = -\dfrac{(u_z^0 - u_{zT}^0)/(L_t^R/2)}{(u_x^* - u_{xT}^*)/(L_l^R/2)}, \end{cases} \tag{18}$$

where σ_{xx}^* is the mechanical mean stress acting on the $x = L_l^R/2$ plane of the RVE, and u_{xT}^*, u_{yT}^0 and u_{zT}^0 are the uniform displacements in the x-, y- and z-directions on the $x = L_l^R/2$, $y = L_t^R/2$ and $z = L_t^R/2$ planes of the RVE under pure thermal load, respectively. The mechanical mean stress σ_{xx}^* is obtained as:

$$\sigma_{xx}^* = \frac{\displaystyle\int_0^{L_t^R/2}\int_0^{L_t^R/2}\sigma_{xx}^M(L_l^R/2,y,z)dydz}{(L_t^R/2)^2}. \tag{19}$$

Transverse normal loading can be simulated by the uniform displacement in the y- or z-direction applied to the boundary of the RVE. An analysis procedure similar to the case of longitudinal normal loading can be employed for the case of transverse normal loading, and the transverse Young's modulus $E_t^R = E_y^R = E_z^R$ and Poisson's ratio $\nu_{tt}^R = \nu_{yz}^R = \nu_{zy}^R$ can be obtained.

For longitudinal shear loading, a whole RVE ($-L_l^R/2 \le x \le L_l^R/2$, $-L_t^R/2 \le y \le L_t^R/2$, $-L_t^R/2 \le z \le L_t^R/2$) was considered. The displacement boundary conditions for the RVE under longitudinal shear are as follows:

$$\left.\begin{array}{l} u_x^M(x,y,-L_t^R/2) = 0, \\ u_y^M(x,y,-L_t^R/2) = 0, \\ u_z^M(x,y,-L_t^R/2) = 0, \\ u_x^M(x,y,L_t^R/2) = u_x^*, \\ u_y^M(x,y,L_t^R/2) = 0, \\ u_z^M(x,y,L_t^R/2) = 0, \end{array}\right\} \quad -\frac{L_l^R}{2} \le x \le \frac{L_l^R}{2}, \ -\frac{L_t^R}{2} \le y \le \frac{L_t^R}{2}. \tag{20}$$

Here, the displacement in the y-direction on the $z = L_t^R/2$ plane of the RVE is arbitrary, so that $u_y^M(x,y,L_t^R/2) = 0$. In addition, points on the $x = -L_l^R/2$ and $x = L_l^R/2$ faces with the same y- and z-coordinates need to be constrained to have the same displacements in all three directions, i.e.,

$$\left.\begin{array}{l} u_x^M(-L_l^R/2,y,z) = u_x^M(L_l^R/2,y,z), \\ u_y^M(-L_l^R/2,y,z) = u_y^M(L_l^R/2,y,z), \\ u_z^M(-L_l^R/2,y,z) = u_z^M(L_l^R/2,y,z), \end{array}\right\} \quad -\frac{L_t^R}{2} \le y \le \frac{L_t^R}{2}, \ -\frac{L_t^R}{2} \le z \le \frac{L_t^R}{2}. \tag{21}$$

The longitudinal shear modulus $G_{lt}^R = G_{tl}^R = G_{zx}^R$ is given by

$$G_{lt}^R = G_{tl}^R = G_{zx}^R = \frac{\sigma_{zx}^*}{u_x^*/L_l^R}. \tag{22}$$

The mechanical mean stress σ_{zx}^* is computed from

$$\sigma_{zx}^* = \frac{\displaystyle\int_{-L_t^R/2}^{L_t^R/2}\int_{-L_t^R/2}^{L_t^R/2}\sigma_{zx}^M(x,y,L_t^R/2)dxdy}{L_l^R L_t^R}. \tag{23}$$

The finite element software, ANSYS 11.0, was used to create and analyze the three-dimensional RVE models for CNT-reinforced composites. The finite element models were meshed with eight-noded brick elements. The typical model ($L^E/2R^E = 50$) for longitudinal and transverse normal load-

ings consists of 13629 nodes and 11552 elements while the model for longitudinal shear loading has 95625 nodes and 92416 elements.

3.3 Randomly oriented CNT-reinforced composite

Figure 4 shows the composite with randomly oriented CNTs. The global Cartesian coordinate system (X, Y, Z) for the composite is also shown in the figure. The components of the effective elastic compliance tensor for the randomly oriented CNT-reinforced composite can be obtained as the average values of the compliance components for the RVE over all orientations defined by the transformation from the local RVE coordinates (x, y, z) to the global composite coordinate system (X, Y, Z).
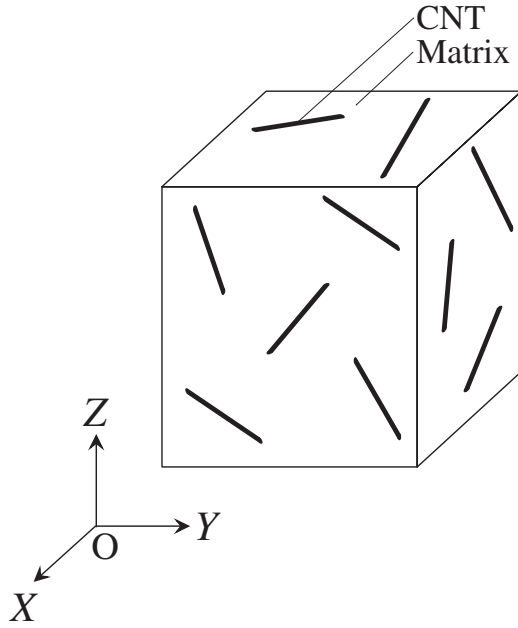
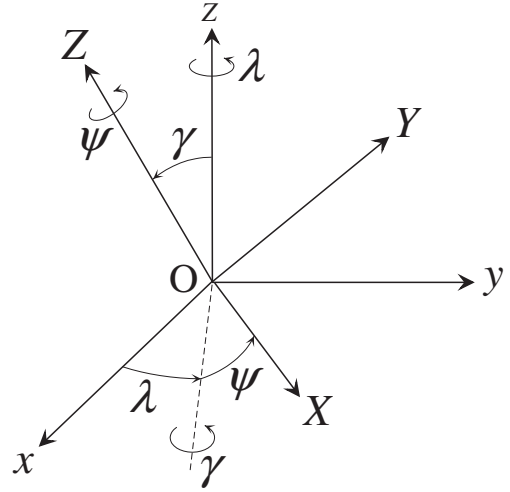Fig. 4   Randomly oriented CNT-reinforced composite.

Fig. 5   Rotation of coordinates.

The elastic compliance components for the transversely isotropic RVE can be expressed in terms of the five independent elastic properties E_l^R, E_t^R, ν_{lt}^R, ν_{tt}^R, $G_{lt}^R = G_{tl}^R$. The non-zero components of the compliance tensor for the RVE, S_{ijkl}^R ($i, j, k, l = 1, 2, 3$), in the coordinates (x, y, z) are given by

$$S_{1111}^R = \frac{1}{E_l^R}, \quad S_{1122}^R = S_{1133}^R = -\frac{\nu_{lt}^R}{E_l^R}, \quad S_{2222}^R = S_{3333}^R = \frac{1}{E_t^R}, \quad S_{2233}^R = -\frac{\nu_{tt}^R}{E_t^R}, \\ 4S_{2323}^R = 2(S_{2222}^R - S_{2233}^R) = \frac{1}{G_{tt}^R} = \frac{2(1 + \nu_{tt}^R)}{E_t^R}, \quad 4S_{1212}^R = 4S_{1331}^R = \frac{1}{G_{lt}^R}. \tag{24}$$

The compliance components satisfy the following symmetry relations:

$$S_{ijkl}^R = S_{klij}^R = S_{jikl}^R = S_{ijlk}^R. \tag{25}$$

The effective elastic compliance tensor for the randomly oriented CNT-reinforced composite (denoted by superscript C) is given by[27]

$$S_{ijkl}^C = \frac{1}{2\pi^2} \int_{-\pi}^{\pi} \int_0^{\pi} \int_0^{\pi/2} a_{ip}a_{jq}a_{kr}a_{ls}S_{pqrs}^R \sin(\gamma) \, d\lambda \, d\gamma \, d\psi, \tag{26}$$

where λ, γ and ψ are the angles indicating the orientation of the global coordinates (X, Y, Z) with respect to the local coordinates (x, y, z) (see Fig. 5), and a_{ij} are the direction cosines for the transformation given by

$$a_{11} = \cos\lambda \cos\psi - \sin\lambda \cos\gamma \sin\psi, \quad a_{12} = \sin\lambda \cos\psi + \cos\lambda \cos\gamma \sin\psi, \\ a_{13} = \sin\psi \sin\gamma, \quad a_{21} = -\cos\lambda \sin\psi - \sin\lambda \cos\gamma \cos\psi, \\ a_{22} = -\sin\lambda \sin\psi + \cos\lambda \cos\gamma \cos\psi, \quad a_{23} = \sin\gamma \cos\psi, \\ a_{31} = \sin\lambda \sin\gamma, \quad a_{32} = -\cos\lambda \sin\gamma, \quad a_{33} = \cos\gamma. \tag{27}$$

The resulting effective elastic compliance tensor for the composite is isotropic. Once the composite compliance tensor is determined, then the two independent effective elastic moduli, i.e., Young's modulus E^C and Poisson's ratio ν^C, of the randomly oriented CNT-reinforced composite can be obtained as follows:

$$E^C = \frac{1}{S_{1111}^C} = \frac{1}{S_{2222}^C} = \frac{1}{S_{3333}^C}, \quad \nu^C = -\frac{S_{1122}^C}{S_{1111}^C} = -\frac{S_{1133}^C}{S_{1111}^C} = -\frac{S_{2233}^C}{S_{1111}^C}. \tag{28}$$

4.   Results and Discussion

4.1   Experiments

Three specimens were tested, and the stress-strain behaviors were very consistent. Figure 6(a) shows typical tensile stress (σ)-percentage strain (ε) curves for the neat polycarbonate and MWNT/polycarbonate composites containing 1.0, 1.7 and 3.4 vol% MWNTs at room temperature (R.T.). Note that strains after the maximum stress were determined based on the testing machine's displacement. Also, the room temperature tests were stopped before specimen failures. At room temperature, the stress-strain curves exhibit considerable nonlinearity before the tensile stress reaches the maximum value. After reaching the maximum stress, a stress
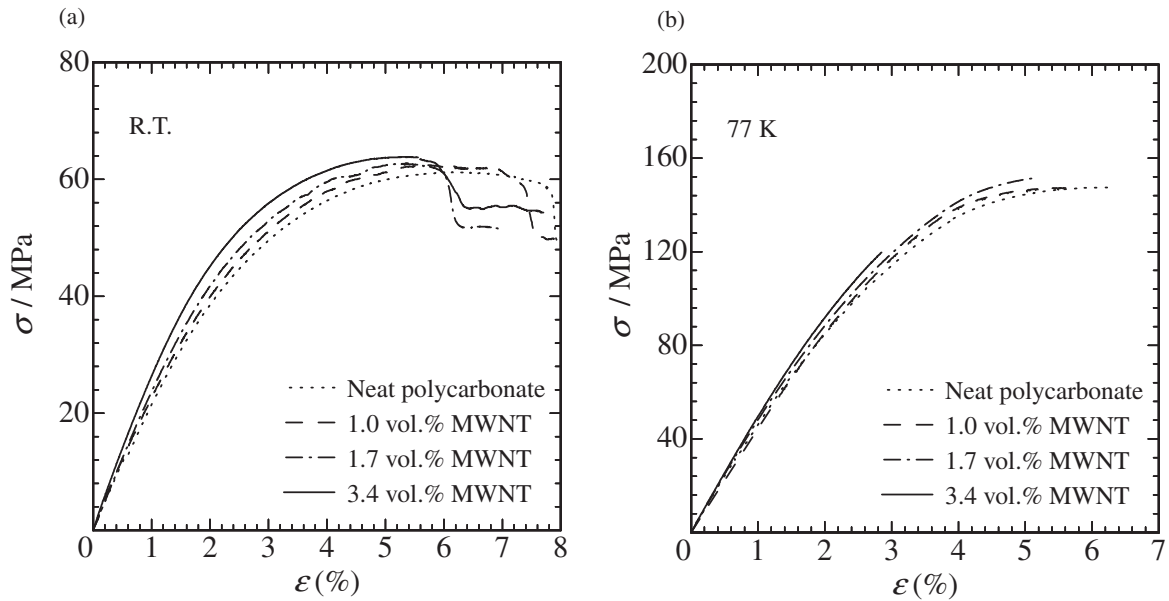
(a)

(b)

Fig. 6   Tensile stress-strain curves from the (a) room and (b) liquid nitrogen temperature tests.

Table 1   Tensile test results.

	Sample	E/GPa	$\bar{E}$/GPa	σ_{YS}/MPa	$\overline{\sigma_{YS}}$/MPa	σ_U/MPa	$\overline{\sigma_U}$/MPa	ε_F (%)	$\overline{\varepsilon_F}$ (%)
R.T.	Neat polycarbonate	2.44	2.35	34.1	34.0	61.0	60.9	—	—
		2.25		34.4		61.2		—	
		2.36		33.5		60.5		—	
	1.0 vol% MWNT	2.44	2.37	35.6	35.7	61.0	61.9	—	—
		2.34		35.3		62.4		—	
		2.34		36.1		62.4		—	
	1.7 vol% MWNT	2.45	2.56	38.5	36.8	63.0	64.6	—	—
		2.54		35.6		65.7		—	
		2.68		36.4		65.0		—	
	3.4 vol% MWNT	2.70	2.63	38.7	40.3	63.8	63.8	—	—
		2.70		39.9		63.7		—	
		2.49		42.4		63.8		—	
77 K	Neat polycarbonate	4.66	4.50	90.1	92.7	148	146	6.33	5.68
		4.43		91.8		141		4.55	
		4.39		96.3		150		6.16	
	1.0 vol% MWNT	4.73	4.44	97.6	96.0	125	140	3.42	4.99
		4.37		94.9		148		5.92	
		4.22		95.4		147		5.64	
	1.7 vol% MWNT	4.55	4.65	105	104	152	152	5.18	5.18
		4.86		102		—		—	
		4.54		104		—		—	
	3.4 vol% MWNT	4.56	4.70	110	105	119	119	3.11	2.98
		4.45		108		120		2.85	
		5.08		97.4		—		—	

drop occurs as a neck forms. Figure 6(b) shows typical tensile stress-percentage strain curves from the liquid nitrogen temperature tests. The curves at 77 K are initially linear and then become nonlinear. At 77 K, all specimens fail immediately after reaching the maximum stress. Table 1 summarizes the Young's modulus E, 0.2% offset yield strength σ_{YS} and ultimate tensile strength σ_U at room temperature and 77 K for all specimens. Also listed are the strain-to-failure ε_F at 77 K in the table. For some specimens tested at 77 K, failure was preceded by slippage between the specimen and grip surfaces, and the ultimate tensile strength and strain-to-failure data could not be obtained. In the table, the overbar represents the average value. The Young's modulus, 0.2% offset yield strength and ultimate tensile strength at 77 K are higher than those at room temperature. The Young's modulus and 0.2% offset yield strength at room
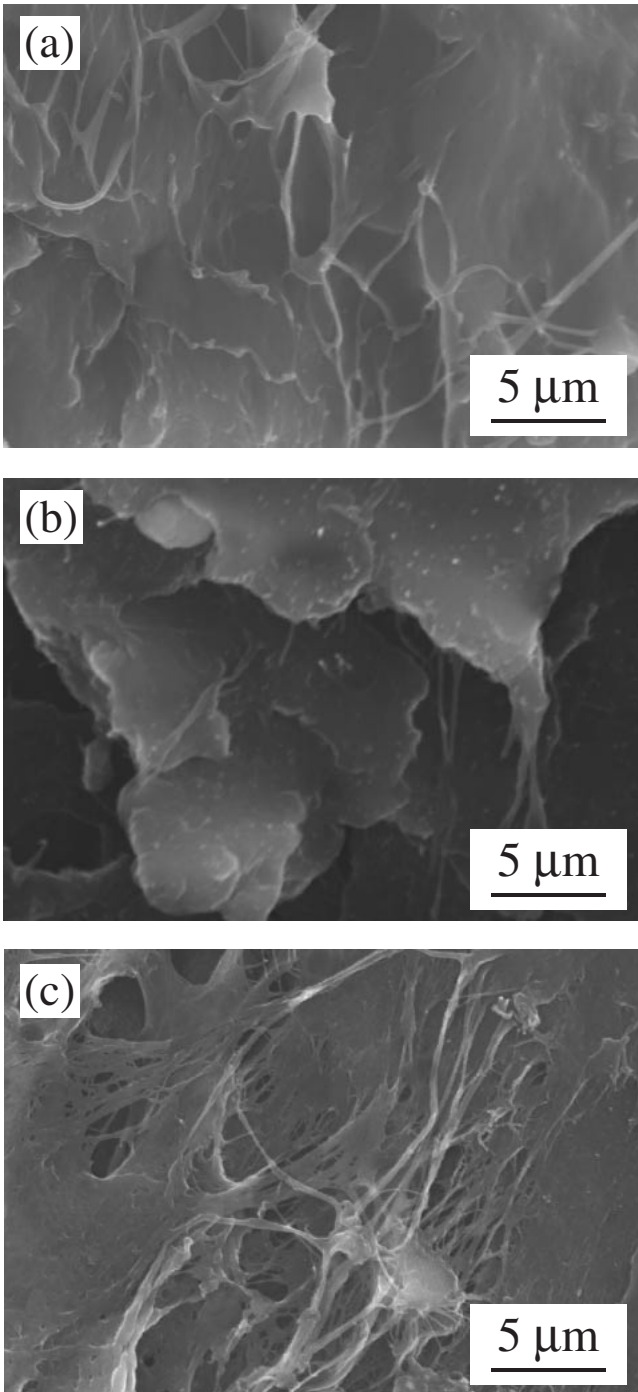
Fig. 7   SEM images of the fracture surfaces for the (a) 1.0 vol%, (b) 1.7 vol% and (c) 3.4 vol% MWNT/polycarbonate composites tested at 77 K.

Table 2   Poisson's ratios of the polycarbonate.

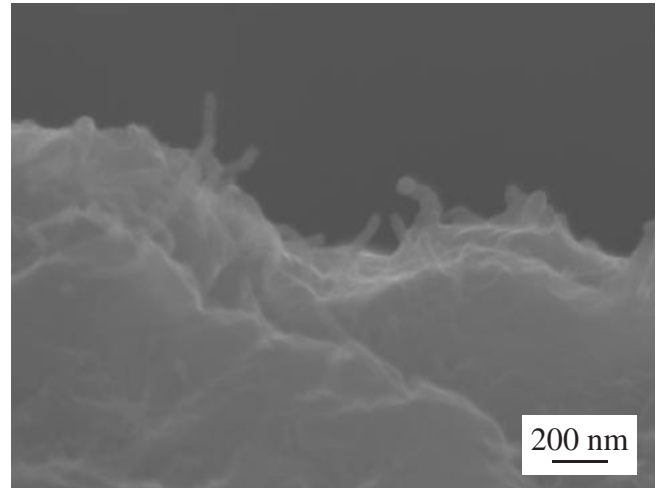|	ν	$\bar{\nu}$
R.T.	0.37	0.39
	0.40	
	0.40	
77 K	0.35	0.38
	0.40	
	0.40	

Fig. 8   Higher magnification SEM image of the fracture surface for the 3.4 vol% MWNT/polycarbonate composite tested at 77 K.

of polymers at cryogenic temperatures.[30] Table 2 lists the Poisson's ratio ν of the polycarbonate at room temperature and 77 K. The Poisson's ratio is almost independent of the temperature. Figure 7 gives the SEM images of the fracture surfaces for the composite specimens at 77 K. MWNT/polycarbonate interface debonding is found, indicating an imperfect interface. Also, the images show that MWNTs are separated into individual tubes and thus well dispersed. Figure 8 shows the higher magnification SEM image of the fracture surface for the 3.4 vol% MWNT/polycarbonate composite specimen at 77 K. The SEM image clearly shows the pulled-out MWNTs. The MWNT pull-out at 77 K was also seen for the composites containing 1.0 and 1.7 vol% MWNTs (no figure shown). For the room temperature tensile test specimens of MWNT/polycarbonate composites, the MWNTs pulled from the fracture surface appeared to be coated by a layer of polycarbonate.[31]

4.2 Multiscale simulations

The predicted Young's modulus E^C of the randomly oriented CNT-reinforced composite is shown in Fig. 9(a) as a function of the effective CNT volume fraction V^E for the parameter $\chi = 1$ (i.e., perfect CNT/matrix interface bonding) at $\Phi = 293$ K (room temperature). The average experimental data for the Young's modulus at room temperature are also plotted in the figure. For the effective CNT aspect ratio $L^E/2R^E$ above 50, the predicted Young's modulus is almost independent of the aspect ratio (no figure shown). Based on this finding, results are presented only for
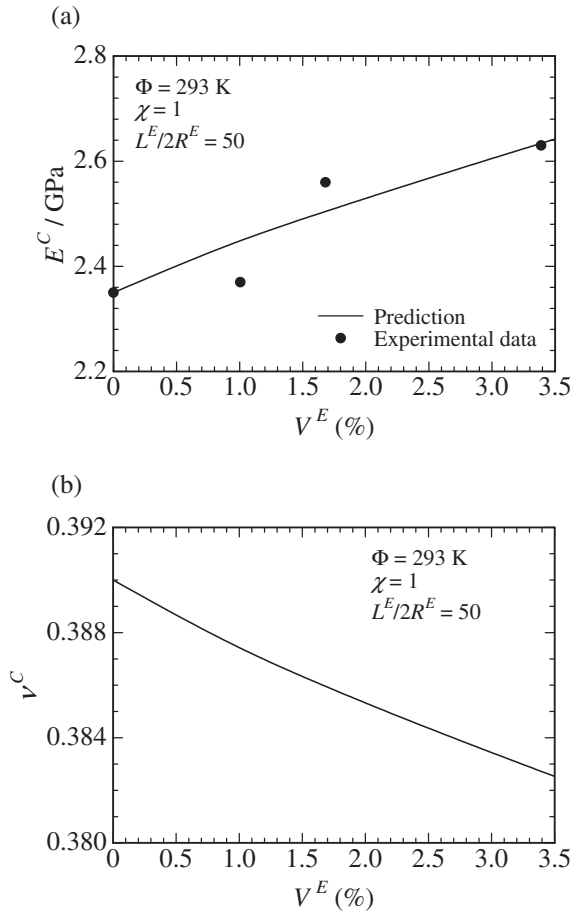
temperature and 77 K increase with increasing nanotube volume fraction. Adding MWNTs in the polycarbonate results in the improvement in ultimate tensile strength at room temperature. It seems that the strain-to-failure at 77 K decreases with increasing nanotube volume fraction. The decrease of strain-to-failure with high nanotube content at 77 K may be attributed to following two effects: first, some defects are produced during nanocomposite fabrication process and the defects increase with the higher reinforcement contents.[28,29] The other one, polymers become very sensitive to the presence of defects, due to the brittleness

(a)

(b)

Fig. 9 Elastic moduli of the randomly oriented CNT-reinforced composite vs. effective CNT volume fraction V^E for $\chi = 1$ and $L^E/2R^E = 50$ at $\Phi = 293$ K: (a) Young's modulus E^C; (b) Poisson's ratio v^C.

(a)

(b)

Fig. 10 Elastic moduli of the randomly oriented CNT-reinforced composite vs. effective CNT volume fraction V^E for $\chi = 1$, 0.05 and $L^E/2R^E = 50$ at $\Phi = 77$ K: (a) Young's modulus E^C; (b) Poisson's ratio v^C.

$L^E/2R^E = 50$. The predicted values of the Young's modulus are in reasonable agreement with the experimental values. The Poisson's ratio v^C of the randomly oriented CNT-reinforced composite at 293 K is shown in Fig. 9(b). The composite Poisson's ratio decreases with the increase in the nanotube volume fraction. This is because the Poisson's ratio of the effective CNT is lower than that of the polycarbonate.

Figure 10(a) shows the predicted Young's modulus E^C of the randomly oriented CNT-reinforced composite as a function of the effective CNT volume fraction V^E for the parameter $\chi = 1$, 0.05 (i.e., imperfect CNT/matrix interface bonding) at $\Phi = 77$ K. A plot of the average experimental data for the Young's modulus at 77 K is also shown in the figure. The analysis for $\chi = 1$ overpredicts the Young's modulus at 77 K. For $\chi = 0.05$, the predictions on the Young's modulus are fairly close to the experimental values. Figure 10(b) shows the predicted Poisson's ratio v^C for $\chi = 1$, 0.05 at 77 K. It is observed that the Poisson's ratio for $\chi = 0.05$ is larger than that for $\chi = 1$.

Figure 11 shows the distributions of the shear stress $|\sigma_{zx}^I|$ in the interfacial layer under pure thermal load along an interfacial line ($2L^E/5 \leq x \leq L^E/2$, $y = 0$, $z = R^E$) for the parameter $\chi = 1$ and the effective CNT volume fraction $V^E = 1.0$, 1.7, 3.4% at $\Phi = 77$, 293 K. There are stress concentrations near the effective CNT ends, and the
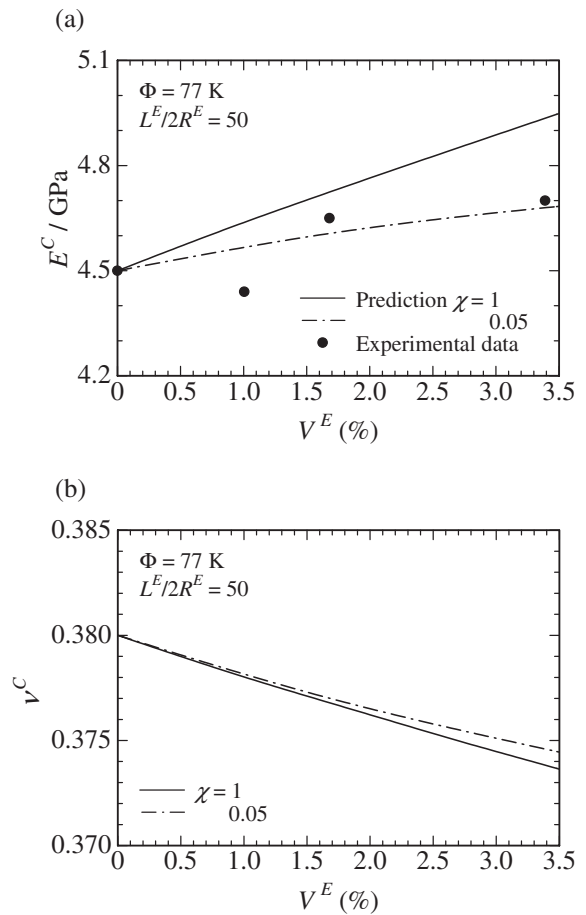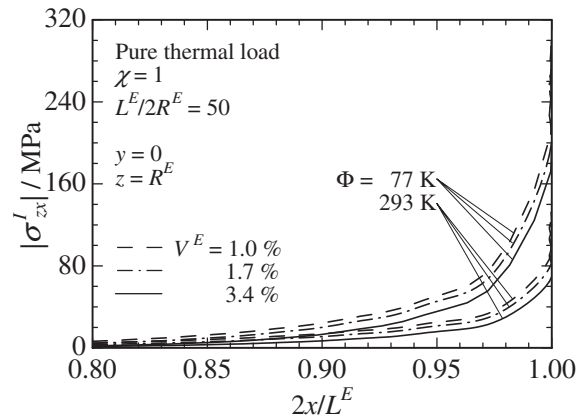

Fig. 11 Distributions of the shear stress $|\sigma_{zx}^I|$ in the interfacial layer under pure thermal load for $\chi = 1$, $V^E = 1.0$, 1.7, 3.4% and $L^E/2R^E = 50$ at $\Phi = 77$, 293 K ($2L^E/5 \leq x \leq L^E/2$, $y = 0$, $z = R^E$).

magnitude of the stress concentrations at 77 K is higher than that at 293 K. Also, the interfacial shear stress increases with the decrease in the nanotube volume fraction. The high interfacial shear stress near the nanotube ends may cause failure of the CNT/matrix interface after the exposure to 77 K.

5. Conclusions

In this work we investigated experimentally and numerically the mechanical performance of MWNT/polycarbonate composites under tension at cryogenic temperatures. The following conclusions based on the tensile tests and the multiscale analysis are briefly summarized below.

(1) The composite properties are affected by the temperature and the addition of the MWNTs.

(2) The interface debonding between the MWNT and the polycarbonate matrix is seen on the fracture surfaces of the composite specimens at 77 K.

(3) The multiscale simulation for the perfect CNT/matrix interface bonding gives a good prediction of the composite Young's modulus at room temperature. In contrast, the Young's modulus at 77 K can be reasonably predicted by the analysis for the imperfect interface bonding.

(4) The high interfacial shear stress near the nanotube ends due to pure thermal load seems to be responsible for the imperfect interface bonding after the exposure to 77 K. The stress analysis results demonstrate the validity of the assumption about the CNT/matrix interface in the Young's modulus prediction.

REFERENCES

1) S. Iijima: Nature **354** (1991) 56–58.
2) M. S. Dresselhaus and P. Avouris: Introduction to Carbon Materials Research, *Carbon Nanotubes: Synthesis, Structure, Properties, and Applications*, ed. by M. S. Dresselhaus, G. Dresselhaus and P. Avouris, (Springer, Berlin, 2001) pp. 1–9.
3) M. Terrones: Annu. Rev. Mater. Res. **33** (2003) 419–501.
4) X.-L. Xie, Y.-W. Mai and X.-P. Zhou: Mater. Sci. Eng. R **49** (2005) 89–112.
5) C. Li and T.-W. Chou: J. Nanosci. Nanotech. **3** (2003) 423–430.
6) R. P. Reed, R. E. Schramm and A. F. Clark: Cryogenics **13** (1973) 67–82.
7) G. Yang, S.-Y. Fu and J.-P. Yang: Polymer **48** (2007) 302–310.
8) K.-T. Lau, S.-Q. Shi and H.-M. Cheng: Comp. Sci. Tech. **63** (2003) 1161–1164.
9) E. T. Thostenson, Z. Ren and T.-W. Chou: Comp. Sci. Tech. **61** (2001) 1899–1912.
10) D. Srivastava, C. Wei and K. Cho: Appl. Mech. Rev. **56** (2003) 215–230.
11) K.-T. Lau, C. Gu and D. Hui: Comp. Part B **37** (2006) 425–436.
12) R. Andrews and M. C. Weisenberger: Curr. Opin. Solid State Mater. Sci. **8** (2004) 31–37.
13) R. D. Bradshaw, F. T. Fisher and L. C. Brinson: Comp. Sci. Tech. **63** (2003) 1705–1722.
14) R. Guzmán de Villoria and A. Miravete: Acta Mater. **55** (2007) 3025–3031.
15) P. M. Ajayan and O. Z. Zhou: Applications of Carbon Nanotubes, *Carbon Nanotubes: Synthesis, Structure, Properties, and Applications*, ed. by M. S. Dresselhaus, G. Dresselhaus and P. Avouris, (Springer, Berlin, 2001) pp. 391–425.
16) ASTM D 638-03, Standard test method for tensile properties of plastics.
17) X.-L. Gao and K. Li: Int. J. Solids Struct. **42** (2005) 1649–1667.
18) K.-T. Lau, C. Gu, G.-H. Gao, H.-Y. Ling and S. R. Reid: Carbon **42** (2004) 426–428.
19) J. R. Xiao, B. A. Gama and J. W. Gillespie Jr.: Int. J. Solids Struct. **42** (2005) 3075–3092.
20) M. S. Dresselhaus, G. Dresselhaus and R. Saito: Carbon **33** (1995) 883–891.
21) B. J. Chen and S. A. Meguid: Int. J. Solids Struct. **44** (2007) 3828–3839.
22) *American Institute of Physics Handbook*, Third edition, (McGraw-Hill, New York, 1972).
23) K. Liao and S. Li: Appl. Phys. Lett. **79** (2001) 4225–4227.
24) A. Levy and J. M. Papazian: Metall. Trans. A **21A** (1990) 411–420.
25) M. W. Hyer: *Stress Analysis of Fiber-Reinforced Composite Materials*, (McGraw-Hill, New York, 1998) pp. 1–38.
26) C. T. Sun and R. S. Vaidya: Comp. Sci. Tech. **56** (1996) 171–179.
27) G. M. Odegard, T. S. Gates, K. E. Wise, C. Park and E. J. Siochi: Comp. Sci. Tech. **63** (2003) 1671–1687.
28) D. Qian, E. C. Dickey, R. Andrews and T. Rantell: Appl. Phys. Lett. **76** (2000) 2868–2870.
29) Y.-K. Choi, Y. Sugimoto, S.-M. Song, Y. Gotoh, Y. Ohkoshi and M. Endo: Carbon **43** (2005) 2199–2208.
30) M. B. Kasen: Cryogenics **21** (1981) 323–340.
31) W. Ding, A. Eitan, F. T. Fisher, X. Chen, D. A. Dikin, R. Andrews, L. C. Brinson, L. S. Schadler and R. S. Ruoff: Nano Lett. **3** (2003) 1593–1597.